Floating particles transport through the free surface vortex technique: A novel numerical study to assess the interaction among different scales of vortex structures

Floating particles transport through the free surface vortex technique: A novel numerical study to assess the interaction among different scales of vortex structures

Zhixiang Li(李志祥)[a,b], Huixiang Chen(陈会向)[a,b], Hui Xu(徐辉)[a,b], Jiangang Feng(冯建刚)[a,b], Mosè Rossi[c], Shangtuo Qian(钱尚拓)[a,b], Zixuan Yang(杨子轩)[d], Kan Kan(阚阚)[b,e,f,*]

[a]College of Agricultural Science and Engineering, Hohai University, Nanjing, 210098, PR China

[b]College of Water Conservancy and Hydropower Engineering, Hohai University, Nanjing, 210098, PR China

[c]Department of Industrial Engineering and Mathematical Sciences (DIISM), Marche Polytechnic University, Ancona, 60131, Italy

[d]Institute of Mechanics, Chinese Academy of Sciences, Beijing, 100190, China

[e]School of Electrical and Power Engineering, Hohai University, Nanjing, 211100, PR China

[f]National Engineering Research Center of Water Resources Efficient Utilization and Engineering Safety, Hohai University, Nanjing, 210098, PR China

[*]Correspondence: kankan@hhu.edu.cn

Abstract: Fat, oil and grease (FOG) floating particles in the sump of sewage pumping stations will accumulate together to form rigid layers, resulting in failure for pump device. To overcome this, the free surface vortex (FSV) technique has been considered and applied to transport floating particles toward the submerged suction pump inlet. This paper investigates the potential of vortices as a means of downward motion of FOG. The entrainment capacity of FSV is investigated by numerical simulations using a coupled level-set and volume-of-fluid method. Two coherent structures are decomposed by proper orthogonal decomposition: FSV represented by the first two orders with high energy content and spiral vortex bands represented by low energy and high order models. The extracted ridges of the finite-time Lyapunov exponent (FTLE) delineate different regions of the flow field and effectively capture the evolution of Lagrangian coherent structures. The floating particles in the sump are first caught by the dividing line formed by the FTLE ridges, mixed in the entrainment zone, and then merged into the vortex. The enstrophy production term dominates the development of vorticity. Subject to the influence of flow velocity gradients, both radial and tangential vortices undergo a transition into axial vortices. This transformation enhances the vortex's capacity to entrain particles within the vortex core area, leading to their rapid inward spiraling towards the vortex center and eventual expulsion due to the vortex's entrainment effect.

Keywords: Free surface vortex; Lagrangian coherent structures; particle dynamics; orthogonal decomposition; sewage pumping station.

1 Introduction

Sewage pumping stations are a major component of sewage services, collecting sewage from urban pipelines via sumps and lifting sewage to higher water levels to assist normal gravity flow in reaching its final destination, a sewage treatment plant. Sewage pumping stations play a crucial role in ensuring urban sanitation and environmental protection. In urban areas across most countries, these stations often encounter challenges associated with the accumulation of floating fat and other debris, collectively referred to as "floating debris" in their sumps. While large floating debris typically gets stacked and filtered out by trash racks before entering the sump, smaller and more pliable floating debris like fat, oil, and grease (FOG) particles might accumulate above the pump intake. Over time, these FOG floating particles undergo a series of chemical and physical transformations until it becomes a rigid layer that covers the entire sump surface.[1] The presence of such rigid layers within urban drainage systems blocks drainage and leads to rainwater and sewage overflow, which can damage sewage system and pose environmental and health risks.[2, 3] As a result, the timely removal of this rigid layer from the sump is crucial for both their correct operation and reliability as well. Nevertheless, this kind of intervention is not only labor-intensive, hazardous, and unhygienic but also cost-consuming. Duinmeijer[4] proposed the creation of FSV within the sump to overcome the criticalities previously mentioned, which are a means of transport for floating particles from the water surface down to the suction pipe. Since vortices have a strong suction capacity for particles.[5]

To evaluate the transport capacity of FSV, it is necessary to understand the three-dimensional flow field information of the vortices. Based on Navier-Stokes governing equations, different vortex theoretical models have been derived to characterize and describe the tangential velocity, the water surface profile, and other parameters such as the Rankine and Burgers vortex models.[6, 7] Starting from these models, the simplified vortex theoretical models have been further improved and assessed through experimental data and then analyzed deeply with computational fluid dynamics.[8] It is all known that the presence of multiple phases and the associated mass transport, including the particle movement and air entrainment, heighten the operational risks faced by pumping stations. Scientists and technicians have focused their studies on establishing relationships between boundary conditions, operational parameters, and the occurrence of FSV to provide a better prediction of such a physical phenomenon. They also investigated the mechanisms underlying the formation of FSV, the rate of air entrainment, and their impact on pump devices. In the investigation of the entrainment of floating particles by FSV, Naderi *et al.*[9] and Duinmeijer *et al.*[10] used high-speed digital cameras to visually track and calculate the trajectories, as well as the three-dimensional velocity components, of particles within FSV. Notably, Duinmeijer and Clemens[2] observed that the motion trajectories of particles driven by FSV exhibit conspicuous chaotic behavior and are highly sensitive to the initial conditions of these particles.

While most of the aforementioned studies have analyzed the motion of individual or multiple particles propelled by FSV, there is a paucity of research delving into the motion of particle swarm and exploring the potential coupling effects among coherent structures induced by these FSVs. At present, the discussions of FSV flow predominantly rely on the Eulerian perspective, which is effective but cannot provide the transport and mixing process of the coherent structures.[11-13] The Lagrangian system of flow structure identification method has gradually developed. It views the flow field as a dynamic system comprising discrete particles and leverages disparities in particle trajectories to identify Lagrangian coherent structures (LCS) within the flow field. Due to its inherently swarm-based nature, which transcends the characteristics of individual particle trajectories, LCS offer precise material transport evaluation and provides powerful opportunities to predict, and even influence, large-scale flow characteristics and mixing events.[14, 15] This paper aims to provide insights into the transport mechanism of FOG particles and the dynamic characteristics of the flow structure, which will aid in making informed decisions regarding operations and management, such as employing FSV for floating particles transport or undertaking manual salvage operations.

While LCS have demonstrated their utility in various geophysical and biomedical applications, their applicability within the context of FSV flows remains unexplored. In this paper, we employ the coupled level-set and volume-of-fluid (CLSVOF) method in conjunction with large-eddy simulation (LES) methods to reproduce the two-phase vortex flow phenomena in the sewage sump. Through proper orthogonal decomposition (POD), the intricate interaction among different-scale vortex structures is unveiled. The entrainment process of particles under the force of FSV and the LCS transport mechanism are further analyzed, which are the key to understanding the hydrodynamic mixing characteristics in the FSV system. The main content of this paper has been structured as follows: Section 2 presents the geometric parameters and the numerical methods; in Section 3, two analysis methods, namely POD and the finite-time Lyapunov exponent (FTLE), are introduced; in Section 4, the analysis of the spiral vortex band, vortex structures, and particle trajectories constitutes the primary research content; lastly, Section 5 gives the main conclusions derived from the research.

2 Numerical model

2.1 Governing equations

Urban sewage pumping stations are composed of submerged-type pumps so that a free surface, which is the interface between water and air, is present above them. When dealing with more than two fluids, numerical simulations of water flow in pumps become a challenging task to deal with, especially when floating particles are grouped on the sump free surface.[16] Therefore, LES combined with CLSVOF to accurately capture the water-air interface, particularly in regions where high curvature deformation occurs, and simulate the coherent structures within the sump. The continuity and momentum equations of LES combined with CLSVOF are the following:

$$\frac{\partial \tilde{u}_i}{\partial x_i} = 0, \tag{1}$$

$$\frac{\partial \tilde{u}_i}{\partial t} + \tilde{u}_j \frac{\partial \tilde{u}_i}{\partial x_j} = -\frac{\partial \tilde{p}}{\rho \partial x_i} + \nu \frac{\partial^2 \tilde{u}_i}{\partial x_j \partial x_j} + \frac{\partial \tau_{ij}}{\partial x_j} + \frac{\sigma \kappa \delta_s n_i}{\rho} - g\delta_{i3}. \tag{2}$$

Here, p is the pressure; u_i stands for the fluids velocity vector; the tilde (~) denotes the filtered quantities in LES governing equations; σ is the surface tension coefficient; δ_{ij} is the Kronecker delta symbol (If $i = j$, $\delta_{ij} = 1$, otherwise $\delta_{ij} = 0$); κ is local mean curvature of the immiscible fluids interface; ρ and ν are the fluids mixture density and dynamic viscosity, respectively; g represents the effect of gravity and is the acceleration of gravity; The subgrid-scale stress τ_{ij} resulting from filtering is calculated by the Boussinesq hypothesis:[17]

$$\tau_{ij} = 2\nu_{SGS}\tilde{S}_{ij} - \frac{1}{3}\tau_{kk}\delta_{ij}, \tag{3}$$

$$\tilde{S}_{ij} = \frac{1}{2}\left(\frac{\partial \tilde{u}_i}{\partial x_j} + \frac{\partial \tilde{u}_j}{\partial x_i}\right), \tag{4}$$

where τ_{kk} is the isotropic part of τ_{ij} and ν_{SGS} is the sub-grid eddy viscosity. The wall-modeled LES (WMLES) method is adopted in the simulation. As opposed to the traditional LES method, WMLES does not need a grid refinement within the boundary layer, thus saving computational efforts.[18, 19] Currently, this method is being used in numerical simulations of two-phase flow [20]. In the WMLES method, ν_{SGS} is calculated by：

$$\nu_{SGS} = \min\left[(0.41d_w)^2, (0.2\Delta)^2\right] \cdot \sqrt{2\tilde{S}_{ij}\tilde{S}_{ij}} \cdot \left\{1 - \exp[-(y^+/25)^3]\right\}, \tag{5}$$

where d_w is the normal distance from the gird node to the wall and y^+ is the dimensionless wall distance for a wall-bounded flow. When calculating the filter size, a wall damping function is introduced in the WMLES method, written as equation (6). Thus, this method is well suited for anisotropic grids reducing the requirement for grids near the wall and improving calculation efficiency:

$$\Delta = \min(\max(0.15d_w, 0.15h_{\max}, h_{wn}), h_{\max}). \tag{6}$$

Here, h_{max} is the longest edge of a hexahedral cell (for other cell types, this concept is extended accordingly). h_{wn} is the grid spacing in the wall-normal direction.

The CLSVOF method has been well applied in simulating vortex phenomena in the sump or pipe.[21, 22] This approach offers an accurate representation of the air-water interface while maintaining mass conservation.[23] The CLSVOF method tracks the interface of immiscible fluids by establishing a convection equation, from which it derives a volume fraction function F and a signed distance ϕ. The signed distance ϕ determines ρ and ν of the immiscible fluids in equation (2):

$$\phi(x,t) = \begin{cases} +|d| & x \in \text{water} \\ 0 & x \in \text{interface} \\ -|d| & x \in \text{air} \end{cases}, \tag{7}$$

$$\rho = \rho_w H(\phi) + \rho_a[1 - H(\phi)], \tag{8}$$

$$\nu = \nu_w H(\phi) + \nu_a[1 - H(\phi)], \tag{9}$$

where d is the distance from the interface. Positive and negative values of ϕ represent water and air phases respectively. $H(\phi)$ stands for the smoothed Heaviside function.[24, 25] All velocities are filtered in the subsequent section, while the tilde (~) is omitted for simplicity.

2.2 Setup of the simulation

Large-scale water supply and drainage pumping stations commonly employ a horizontal inflow configuration.[26] As shown in Fig. 1, this layout simplified an inflow system with a horizontal pipe as a water inlet,[27, 28] where D = 0.4 m is the pipe mouth diameter. The submergence hs and the suspended height of the pipe mouth are 1.5D and 1.0D, respectively. To minimize the interference of domain inlet boundary on the flow near the pipe mouth, the maximum edge length for the sump is set to 12.0D. The coordinates origin is established at the pipe mouth center. The main flow direction coincides with the positive direction of the x-axis.

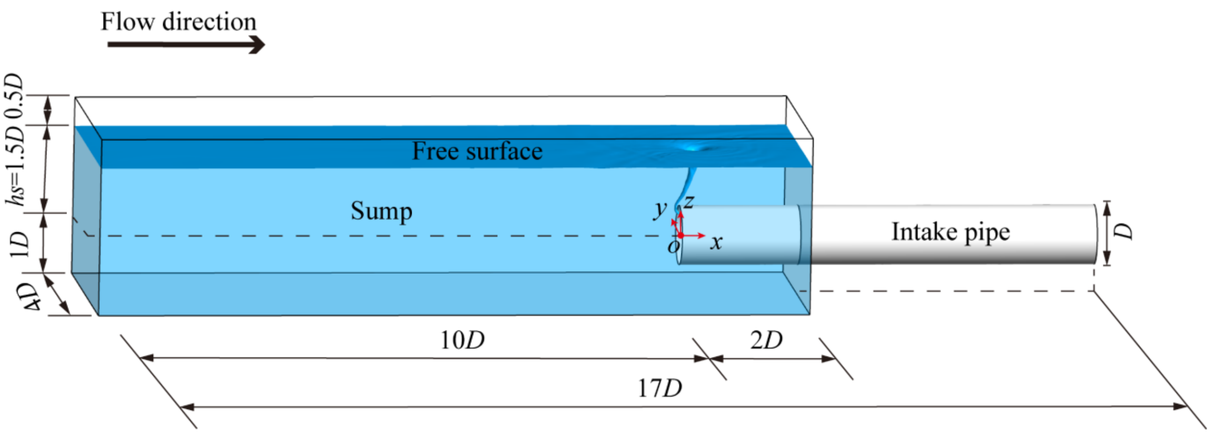

Fig.1. Sketch of the sump model in a drainage pumping station.

The calculation conditions settings are shown in Table 1, where Q is the discharge. $Fr = u_D / \sqrt{gD}$, $Ds = Q / g^{0.5} hs^{2.5}$, $Re = u_D D / \nu$, and $We = \rho u_D D / \sigma$. Ds is the discharge-to-submergence ratio, quantifying the relationship between Q and hs.[20] Taking Case M3 as an illustrative example, the corresponding boundary conditions have been defined as follows: the upper section of the sump is defined as an opening surface with an atmospheric pressure. The walls of the sump and intake pipe have been configured as non-slip walls. The pipeline outlet employs a pressure outlet that adjusts in real-time with variations in the flow rate. When the discharge overcomes the expected value, the outlet pressure increases, and conversely, it decreases to maintain a steady discharge of $0.785 u_D D^2$ throughout the computation process. The inlet of the sump adopts the air-water two-phase flow inlet. Pure water inlet ($\phi > 0$) is below z = 1.5D with a pressure distribution conforming to the hydrostatic pressure. Above z = 1.5D, identical settings equal to the upper section have been applied.[29, 30] The LES simulation employed a time step of $6.41\times10^{-3}D/u_D$, with up to 20 iterations per step. The governing equation discretization is detailed in our previous studies.[20, 31] The simulations of FSV were executed utilizing FLUENT 18.0 software, requiring an extensive computational time of approximately 210,000 CPU hours to complete.

Table 1 Parameters for FSV flow simulation cases.

Case Name	Q/u_DD^2	hs/D	Ds	Fr	Re	We
M1	0.392	1.50	0.21	0.75	5.88×10^5	1.82×10^4
M2	0.785	1.75	0.29	1.49	1.18×10^6	4.86×10^4
M3	0.785	1.50	0.43	1.49	1.18×10^6	4.86×10^4
M4	0.785	1.25	0.67	1.49	1.18×10^6	4.86×10^4
M5	1.375	1.50	0.75	2.62	2.06×10^6	1.49×10^5

2.3 Validation of numerical results

ICEM has been used to mesh the entire computational domain, where the vortex generation region is refined. Grid independence analysis has been performed using the widely accepted GCI criterion.[32, 33] In FSV flow, vertical vorticity ω_z is the important characteristic parameter and is chosen as the evaluation parameter for the grid convergence analysis. Three sets of grid schemes, ranging from fine to coarse (G1 = 17,456,622; G2 = 8,645,974; G3 = 4,224,656) are designed for grid error analyses. The convergence index GCI_{fine}^{21} of ω_z has fallen below 3%, signifying that the refinement of Grids G1 and G2 adequately meets the required convergence criterion.[31, 34] Grid G2 has subsequently been selected for the simulations due to its computational efficiency, as depicted in Fig. 2.

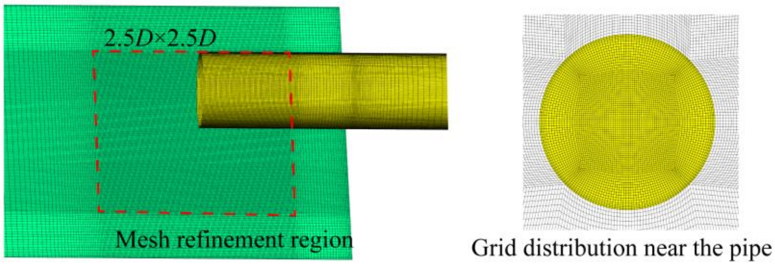

Fig. 2. Mesh generation of Grid G2.

Fig. 3 presents the comparison of the air-water interface between the experimental result from Möller *et al.*[35] and the simulation result. The representation of the free surface is achieved using $F = 0.5$. In general agreement with the results of experiment, numerical calculation effectively captures the overall air-water interface shape as it develops from the water surface to the pipe mouth. The upper part of FSV forms a funnel shape structure, with its central part resembling an elongated air tube, while the tail transitions into a pronounced hook-shaped pattern. The simulation employed a higher flow rate compared to the experimental setup, resulting in the formation of a more pronounced vortex and an increased diameter of the air tube.

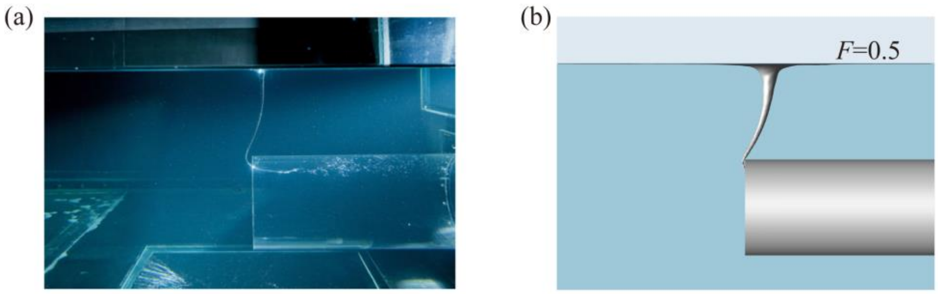

Fig. 3. Comparison of free surfaces: (a) experimental picture from Möller *et al.*[35] and (b) $F = 0.5$ iso-surface of Case M3.

Fig. 4(a) presents the comparison of tangential velocities distribution of FSV between the simulation, experiment, and the theoretical results. Burgers vortex model has been selected as the theoretical model, given its well-verified accuracy in representing tangential velocity according to previous experiments.[36] The graph demonstrates that the calculation result is consistent with Burgers theoretical model. Tangential velocity V_θ increases approximately linearly for radius as $r/r_c < 1$, and then slowly decreases. r_c denotes the radius of the vortex core with maximum V_θ. Considering the primary focus on particle transport and mixing mechanisms, it is imperative to compare the differences in particle trajectories between the experiment and simulation results, as plotted in Fig. 4(b). It illustrates that the particle motion trajectories, which are obtained from the simulation results closely correspond to the measured trajectories from the experiment, while some deviation exists due to the different arrangement of the intake pipe in the experiment that is situated at the bottom, unlike in the simulation case.

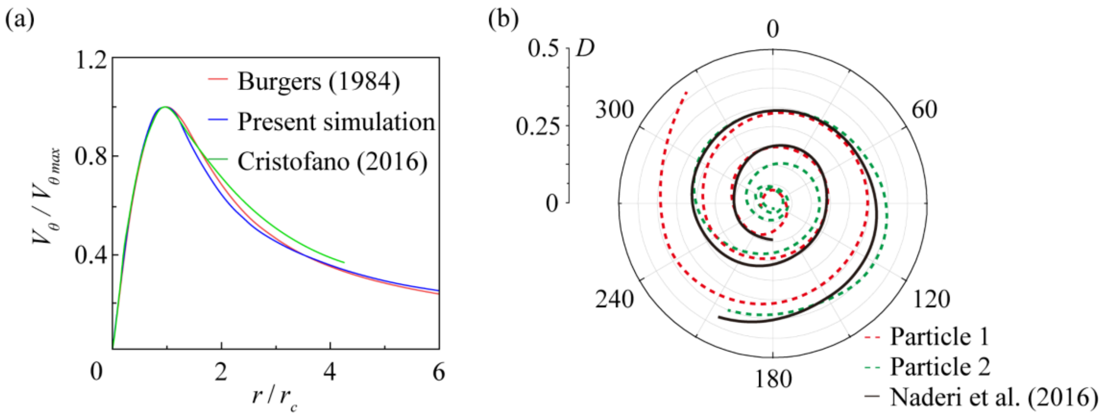

Fig. 4. (a) radial profiles of the tangential velocity and (b) particle trajectories from experiment and simulation results.

3 Coherent structure analysis

3.1 POD analysis

Proper orthogonal decomposition (POD) is a data processing technique commonly employed for analyzing large volumes of data obtained from experiments or numerical simulations of unsteady flow fields. POD decomposes these physical quantities into a series of orthogonal basis functions, referred to as "POD modes", that are optimal in a least-squares sense. Each mode is associated with eigenvalues that represent its energy content. Due to the ability to establish correlations between coherent structures and the energy they encompass, POD has been used to identify structures at different energy levels within turbulent flows. With respect to the motion of particles within the flow field, various flow structures (coherence structures) serve as carriers to determine particle trajectories.

Currently, the most widely used POD method, based on the snapshot method introduced by Sirovich[37], is a mathematical improvement over direct POD that addresses the challenge posed by large spatial point datasets where the spatial correlation matrix cannot be efficiently computed due to the sheer number of spatial points. The snapshot POD method is particularly well-suited for Particle Image Velocimetry (PIV) experiments and numerical simulations, where the count of spatial points m substantially exceeds that of sampling points n.

The central idea of the snapshot POD method is to express the pulsation of a certain physical quantity as the product of a few POD bases $\boldsymbol{\varphi}_j$ and time modal coefficients $a_j(t)$ through the orthogonal decomposition:

$$\boldsymbol{X}' = \sum_j a_j(t)\boldsymbol{\varphi}_j \,, \tag{10}$$

$$\boldsymbol{X}' = \boldsymbol{X} - \bar{\boldsymbol{X}} \,. \tag{11}$$

Here, $\boldsymbol{X} = \left[\boldsymbol{x}(t_1) \quad \boldsymbol{x}(t_2) \quad \dots \quad \boldsymbol{x}(t_m)\right] \in \mathbb{R}^{n\times m}$ donates instantaneous physical field at m moments and $\bar{\boldsymbol{X}}$ is it's the average part. The eigenvector $\boldsymbol{\psi}$ and its corresponding eigenvalue λ of the constructed covariance matrix $\boldsymbol{X}^T\boldsymbol{X}$ can be solved:

$$\boldsymbol{X}'^T\boldsymbol{X}'\boldsymbol{\psi}_j = \lambda_j\boldsymbol{\psi}_j \,, \tag{12}$$

where the symbol T indicates matrix transposition. The mode of the snapshot POD method can be solved as:

$$\boldsymbol{\varphi}_j = \frac{1}{\sqrt{\lambda_j}}\boldsymbol{X}'\boldsymbol{\psi}_j \,, \tag{13}$$

and time modal coefficient can be written as:

$$a_j(t) = \left\langle \boldsymbol{X}'(t), \boldsymbol{\varphi}_j \right\rangle . \tag{14}$$

POD modes are organized in descending order based on their associated eigenvalues. The energy fraction of a specific POD mode, relative to the total resolved energy, is proportional to its corresponding eigenvalue.[38] Typically, the first k-order modes, whose energy is close to the overall kinetic energy of the flow field, are selected for analysis as follows:

$$\sum_{j=1}^{k}\lambda_j \Big/ \sum_{j=1}^{m}\lambda_j \approx 1 \,. \tag{15}$$

3.2 Lagrangian approach

This paper focuses on the dynamic process of FOG floating particles entrainment by vortices, a phenomenon predominantly governed by vortex structures. Most of the vortex feature extraction approaches are based on the Euler framework for analyzing vortices in unsteady flow fields, but these methods often lack a strict physical interpretation.[14] In contrast, Lagrangian approaches exploit properties of fluid particle trajectories to identify coherent structures.[14, 39] On the contrary, Lagrangian approaches offer objectivity, incorporate flow history information, and provide a clear physical interpretation. The finite-time Lyapunov exponent (FTLE) serves as a widely used method for identifying Lagrangian coherent structures (LCS) within velocity fields that are spatially and temporally discretized across domains with finite spatial and temporal dimensions. The "ridge" structure formed by the maxima in the FTLE field effectively reveals hidden coherent structures. Importantly, LCS does not necessitate artificial threshold value settings, unlike vortex criteria based on the Euler framework that heavily relies on threshold values. f-FTLE and b-FTLE can be obtained by integrating in the forward and backward time directions, respectively. Between them, the ridge of b-FTLE reveals the flow structures.[40, 41] Ridges in the b-FTLE field can visually attract materials or unstable manifolds. In other words, along these ridges, fluid particles experience elongation when their trajectories are traced backward in time. To illustrate the entrainment within the vortex, the FTLE related to attracting material lines has been computed as depicted in Fig. 7.

A two-dimensional flow field represented by a transient velocity field $v(x,t)$, is known over a finite time interval [t_0, t_1]. The movement of fluid particles can be described by the following differential equation:[15]

$$\dot{x} = v(x,t), \tag{16}$$

where trajectories of fluid particles are represented by $x(t; t_0, x_0)$, t_0 stands for initial time and x_0 referring to initial positions. The displacement field $x(t; t_0, x_0)$ maps the movement from the initial positions x_0 to the current positions x over the time interval [t_0, t]. At position x_0, the right Cauchy–Green strain tensor $C_{t_0}^{t}$ is adopted to capture the stretch induced by the velocity gradient, which is written as:

$$C_{t_0}^{t}(x_0) = \left(\frac{\partial x(t;t_0,x_0)}{\partial x_0}\right)^T \left(\frac{\partial x(t;t_0,x_0)}{\partial x_0}\right). \tag{17}$$

$C_{t_0}^{t}$ has two positive eigenvalues. The larger of the two eigenvalues λ_2 represents the maximum extension of the particle, and its corresponding eigenvector indicates the direction of the deformation. Following Haller[39], the FTLE for a period of time [t_0, t_1] is defined as:

$$\text{FTLE}_{t_0}^{t_1}(x_0) = \frac{1}{|t_1 - t_0|} \log \sqrt{\lambda_2 \left[C_{t_0}^{t_1}(x_0) \right]} \tag{18}$$

4 Results and analyses

4.1 Spiral vortex band

Fig. 5 shows the vertical vorticity distribution on the horizontal plane $z = 0.9hs$ under various operating conditions at different discharges and submergences in the sump. Plane $z = 0.9hs$ is selected as the characteristic plane because the vortex behavior on this particular plane exhibits a relatively stable pattern and can also well reflect the flow structure beneath the surface.[24, 35] Notably, the velocity vectors in Figs. 5(a)-(d) depict the counterclockwise rotation of all the vortices, while in Fig. 5(e) the vortex rotates clockwise. Provided that the inlet/outlet boundaries, as well as the sump geometric model, are entirely symmetrical, the FSV rotation direction is random. For ease of discussion and comparison, the vertical vorticity values for Case M5 in Fig. 5(e) have been inverted. In all subplots, the maximum value of the vertical vorticity is focused at the vortex center, while in a specific region outside the center, the vorticity approaches zero. The velocity vector diagrams reveal the presence of a spiral vortex band surrounding the FSV in regions where the water flow convergence or significant flow velocity gradient changes occur. These bands originate either at the side wall or at the confluence points of water flows, spiral in alignment with the rotational direction of FSV, and ultimately converge into it. There are counter-rotating vortices in the vortex band opposite to the vorticity of FSV. As *Ds* increases, both the extent and intensity of the spiral vortex bands increase as well.

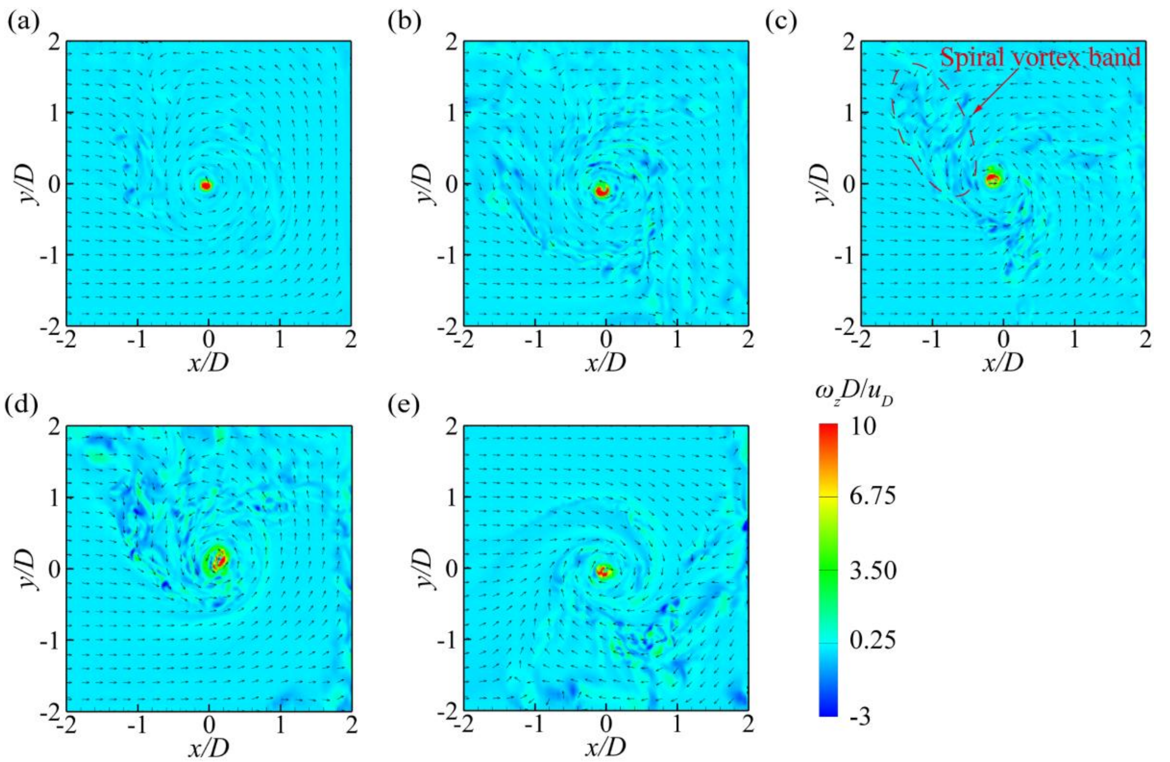

Fig. 5. Distribution of vertical vorticity around FSV: (a) M1, *Ds* = 0.21; (b)M2, *Ds* = 0.29; (c) M3, *Ds* = 0.43; (d) M4, *Ds* = 0.67 and (e) M5, *Ds* = 0.75.

4.2 POD analyses of FSV flied

Following the analysis of the vorticity distribution on the characteristic planes under various flow parameter conditions reported in Section 4.1, it has been determined that there are consistent flow phenomena among them. As a result, Case M3 has been selected as a representative case. To analyze various coherent structures and their transport regions in the suction vortex flow, the transient vertical vorticity of the characteristic plane is selected as the physical quantity for the POD method, and the decomposition results are shown in Fig. 6. Precisely, Fig. 6(a) presents the time-averaged vertical vorticity with a legend that is consistent with the one of Fig. 5. The POD modal eigenvalues calculated with different numbers of snapshots are plotted in Fig. 6(b). POD results are sensitive to the number of snapshots. Generally, eigenvalues exhibit rapid decay as the modal order increases, and then the decay becomes more gradual when the mode order exceeds 12. Comparing 800 and 1,000 snapshots, eigenvalues from both sets are consistent, indicating that the increase in the number of snapshots does not significantly alter the decomposition results. Therefore, POD results obtained from 1,000 snapshots have been chosen for further analysis. The first two modes have the largest eigenvalues and carry the most energy accounting for 32.9% and 17.2% of the total energy, respectively. As the mode order increases, the energy carried by the third and fourth modes decays by 10.1% and 7.1%, respectively. The energy carried by higher-order modes, such as the 9th and 16th modes, is even lower and essentially negligible.

To further explore the relationship between POD modes and vortex structures of various spatial scales within the flow field, the first four high-energy modes were plotted, as well as the 9th and 16th modes in Fig. 6(c). In the first mode, it can be noticed that there is a pair of counter-rotating vortices at the position of FSV, which is approximately distributed in a symmetrical manner along the spanwise direction. In the second mode, the vortex pair rotates almost 90°, parallel to the main flow direction. These findings are consistent with those from POD analyses performed on trailing vortices from wings and inlet vortices from engines.[38, 42, 43] They argued that the first two modes are strongly correlated with the displacement of the vortex; however, when pioneers explained the physical meaning of higher-order modes, they tended to downplay the effect of these modes due to their lower energy content, as depicted in Fig. 6(b). Nevertheless, even though the energies associated with higher-order modes are lower compared to the previous modes, they represent the patterns of small-scale coherent structures near the FSV in the sump. Moving from the first mode to the fourth mode, it is clear that the absolute value of ω_z at the location where the spiral vortex band is situated in Fig. 5 gradually increases with the increasing order of modes. This trend is especially pronounced in the high-order mode (16th mode) where the vortex distribution within the spiral vortex bands closely resembles the results of POD decomposition observed in a von Kármán vortex street. In these regions, small-scale vortices form spiral vortex bands and gradually converge toward the center under the rotational influence of FSV. Consequently, each order mode in the POD results effectively represents different-scale coherent structures that act as carriers for floating particles in the flow field.

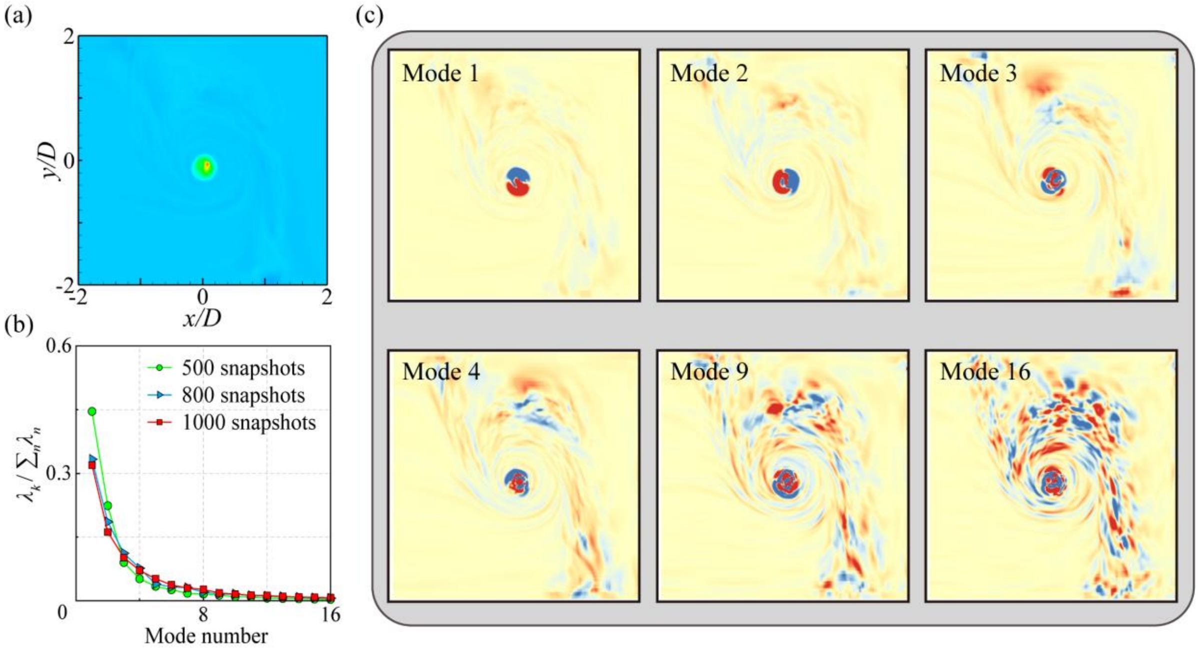

Fig. 6. POD analysis of FSV flow: (a) time-average vortical vorticity flowfield; (b) relative energy fluctuations captured by the POD modes, and (c) first four dominant POD modes, 9th and 16th POD modes.

4.3 Lagrangian analysis

4.3.1 FTLE fields

While vortex bands are discernible in Fig. 5, it is crucial to notice that the selection of the threshold in the Euler method, which employs vorticity for vortex identification, plays a pivotal role in displaying the vortex morphology. This choice heavily relies on the sensitivity and experience of the researcher regarding vortex-related issues. Additionally, as it is clear in Figure 5, despite the author's efforts to optimize the vorticity display range, both the vortex motion patterns and boundaries of the vortex bands appear somewhat blurred. Although the POD decomposition can effectively decompose vortices of different scales (as shown in Fig. 6), the calculation process is relatively complex and depicts their instantaneous evolution. To this end, it is imperative to employ the FTLE method to capture the LCS within the FSV flow field. This approach allows the examination of the overall geometric structure of the vortex flow and provides a precise quantification of the flow characteristics of vortices at various scales, as well as a thorough analysis of the nearby particle transport and mixing processes.

Fig. 7 shows instantaneous FTLE fields on the characteristic plane. The dividing line formed by the upper and lower ridges surrounding the vortex center divides the flow field into two parts: the upstream main flow (Region A) and the reflected flow from the back wall (Region B). The material flux is very small at the clear dividing line formed by the flows on both sides, where the material and energy located in Region A will not cross the dividing line into Region B. This finding aligns with the research conducted by Shadden *et al.*[44] that analyzed observational data of coastal flows through LCS and identified separation areas in ocean currents, namely inner and outer circulation. It is worth highlighting that particles within the water tend to converge towards nearby FTLE ridges and are often captured by them. Comparing the results of the POD analysis in Fig. 6, the ridges of the FTLE field clearly delineate the boundaries of energetic regions, which shows that the FTLE ridges can describe the energy transport pattern carried by the coherent structure in the FSV field. Figs. 7(a-e) show the vortex structure rolled up in the main flow direction. With the entrainment of FSV, it gradually enters the center. When the elliptical LCS (marked with a black circle in Fig. 7(a)) approaches the vortex, the flow velocity increases and the structure is stretched to become flatter, as depicted in Fig. 7(c). As the LCS progress towards the FSV center, it undergoes further stretching, eventually forming a long and narrow spiral line that merges into the FSV center, as seen in Fig. 7(e). In Figs. 7(a-c), the coherent structure remains relatively stable, whereas in Figs. 7(d-e) its shape is influenced by the FSV, thus leading to the gradual disappearance of the LCS structure. Similarly, Figs. 7(e-h) show the evolution of LCS in the backflow from the back wall, which is consistent with the LCS evolution in Region A. In summary, FTLE clearly shows the characteristics of the formation and evolution of the LCS due to the roll-up of FSV existing in the pumping station sump, which can provide insights into the transport mechanisms of coherent structures.

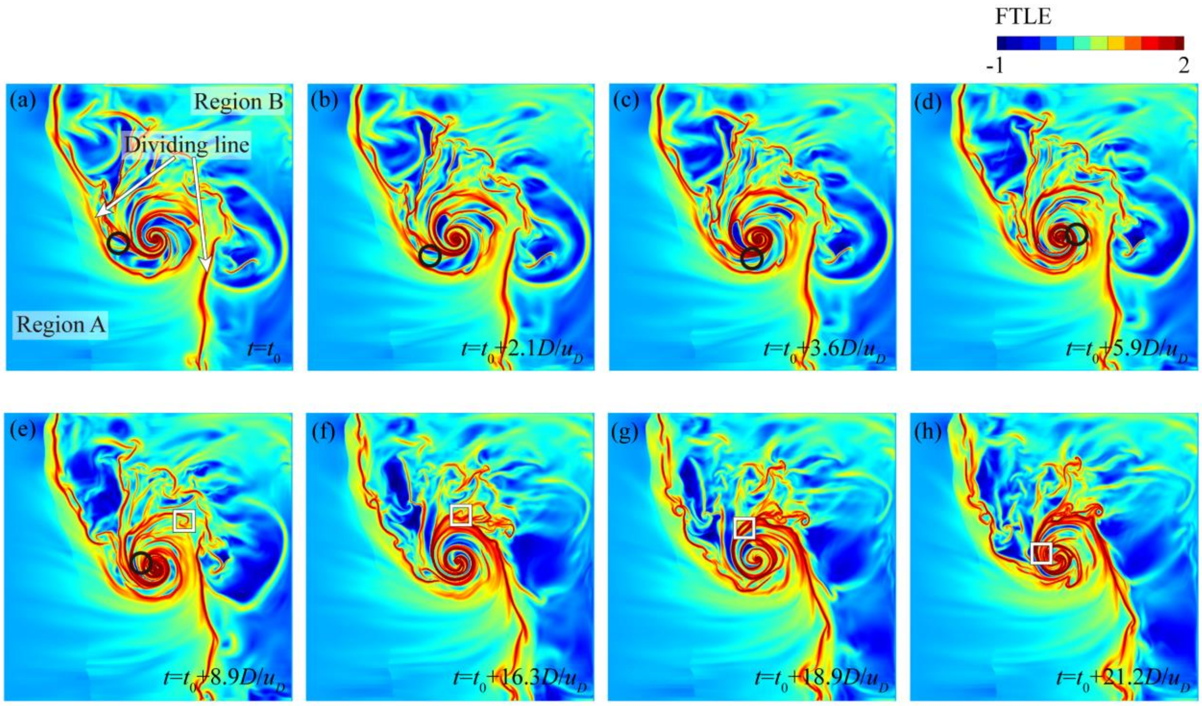

Fig. 7. Instantaneous FTLE flow fields.

4.3.2 Transport process based on trajectories

From the evolution of the aforementioned LCS, the coherent structures undergo significant stretching, resulting in significant alterations in the shape and intensity of the vortex. Enstrophy $\omega^2/2$ can represent the vortex intensity. To examine the dynamics of the vortex, the enstrophy transport equation is utilized, expressed as:[45]

$$\frac{\mathrm{D}\omega^2/2}{\mathrm{D}t} = \omega_i\omega_j\frac{\partial u_i}{\partial x_j} + \nu\nabla^2\omega^2/2 - \nu\frac{\partial\omega_i}{\partial x_j}\frac{\partial\omega_i}{\partial x_j}\,. \tag{19}$$

On the right hand of the equation, the first term represents the effects of the production term, due to the vortex stretching and tilting. The second term accounts for the effects of viscous diffusion, and the third term represents the viscous dissipation of the fluids.

From the Lagrangian perspective, the motion trajectories of particles at different positions in the system are captured and plotted in Fig. 8(a). Green points donate the initial locations of particles. The trajectories of particles illustrate how floating particles, represented by particles with good water flow followability, are entrained by FSV within the sump. Particles from the inflow and those from the backflow mix together in the entrainment zone. Comparing the FTLE field in Fig. 7, it is evident that the entrainment zone is actually a strip region with the dividing line as the bone line. Sultana *et al.*[46] showed that more than 85% of the FOG particles were between 373-2280 μm in size. Consequently, in this study, the behavior of FOG particles in the sump has been represented with fluid particles. While there may be deviations, this approach effectively models the dynamic process of the vortex entrainment of FOG particles, as tested in previous researches.[4, 47, 48] When FSV entrains FOG particles within the sump, particles from different areas initially converge along the dividing line formed by the FTLE ridge, mixing within the entrainment zone. Subsequently, these particles follow the FTLE ridges, spiraling into the vortex at the center of the sump and ultimately being drawn into the suction pipe along with the movement of FSV.

In Fig. 8(a), two trajectories, each marked with a different color, are selected to compare the variations in each term of the equation (18) along distinct pathways. The horizontal axes T^* in Figs. 8(c) and (d) represent the non-dimensional time, which has been normalized by the time required for each particle to move to the center of the vortex. In Fig. 8(c), it is observable that, throughout much of the particle entrainment process, each term of the enstrophy transport equation remains relatively constant. Once the particle enters the vortex core region, as depicted in Fig. 8(b), the production term begins to rise rapidly, while the other two do not exhibit significant changes. This distinction indicates that only the vortex core region, representing the rotational motion of a rigid body, contributes to the propagation of the vortex. The stretching and tilting effects of the vortex represented by the production term are the primary factors contributing to the increased intensity of the vortex. The budgets and the mechanisms described next are found to be the same along the two trajectories, so only the yellow one is further analyzed.

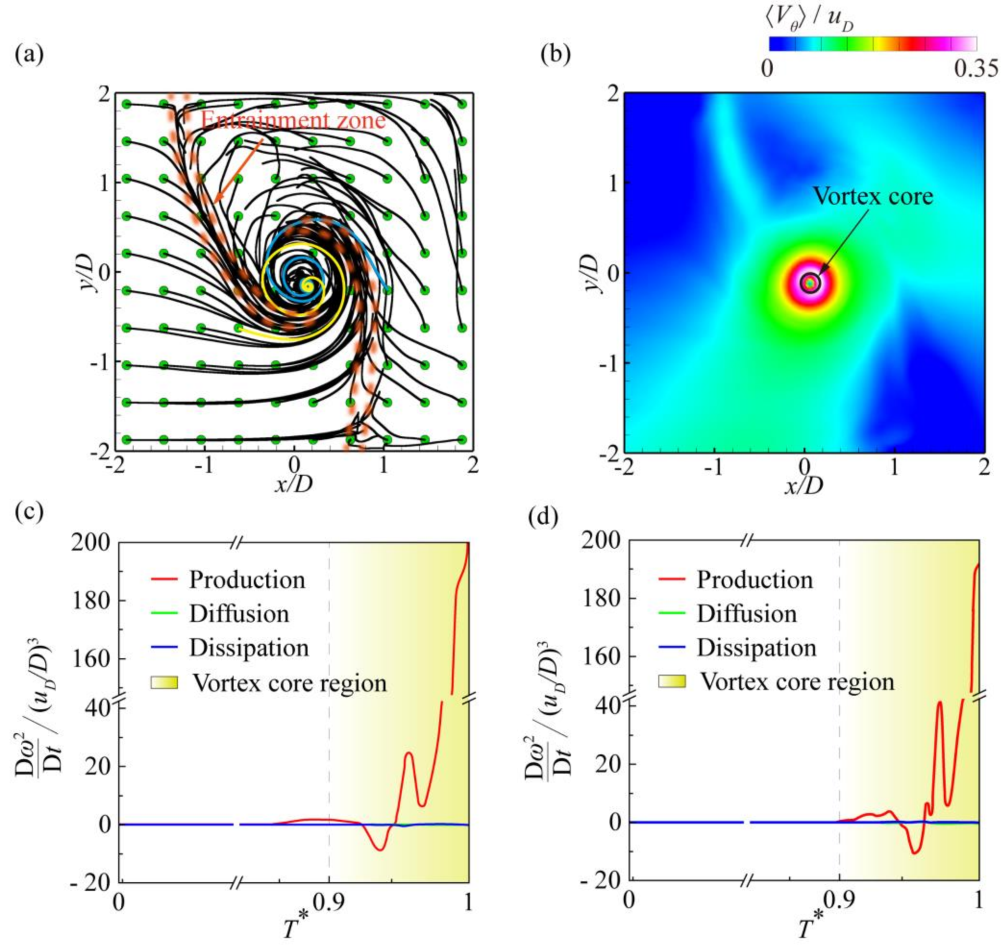

Fig. 8. Trajectories analysis based on Lagrangian perspective: (a) trajectories of the particles entrained into FSV; (b) the tangential velocity contour; (c) enstrophy budget of the trajectory of Particle A (yellow) and (d) enstrophy budget of the trajectory of Particle B (blue).

From the Lagrangian perspective, the variation in the three terms of the enstrophy transport equation is analyzed, concluding that the dominant term is the production one. Given the rotational symmetry of the vortex flow, it becomes challenging to concisely analyze each term of the equation within the Cartesian coordinate system. Consequently, FSV from the Cartesian system is translated into the cylindrical coordinate system. This conversion facilitates a more effective analysis of both primary and secondary components of each term. The expanded form of the production term in the cylindrical coordinate system includes:

$$P_{\omega}=\begin{bmatrix}P_{\omega 1}\\P_{\omega 2}\\P_{\omega 3}\end{bmatrix}=\begin{bmatrix}\omega_r\omega_r\dfrac{\partial V_r}{\partial r} & \omega_r\omega_\theta\left(\dfrac{\partial V_r}{r\partial\theta}-\dfrac{V_\theta}{r}\right) & \omega_r\omega_z\dfrac{\partial V_r}{\partial z}\\ \omega_\theta\omega_r\dfrac{\partial V_\theta}{\partial r} & \omega_\theta\omega_\theta\left(\dfrac{\partial V_\theta}{r\partial\theta}+\dfrac{V_r}{r}\right) & \omega_\theta\omega_z\dfrac{\partial V_\theta}{\partial z}\\ \omega_z\omega_r\dfrac{\partial V_z}{\partial r} & \omega_z\omega_\theta\dfrac{\partial V_z}{r\partial\theta} & \omega_z\omega_z\dfrac{\partial V_z}{\partial z}\end{bmatrix}, \tag{20}$$

where the subscripts 1-3 of P_ω represent the radial r, tangential θ, and axial z direction components in the cylindrical coordinate system, respectively. The transformations between the variables of cylindrical and Cartesian coordinate systems read as:

$$\begin{bmatrix} V_r \\ V_\theta \\ V_z \end{bmatrix} = \begin{bmatrix} \cos\theta & \sin\theta & 0 \\ -\sin\theta & \cos\theta & 0 \\ 0 & 0 & -1 \end{bmatrix} \begin{bmatrix} u \\ v \\ w \end{bmatrix}, \tag{21}$$

$$\theta = \tan^{-1}\left(\frac{y-y_0}{x-x_0}\right). \tag{22}$$

Here, (x_0, y_0) is the FSV coordinate. Fig. 9(a) illustrates the variation in the production term across the three directional components along the particle trajectory. The axial component of the production term ($P_{\omega 3}$) is particularly significant and exhibits a high degree of similarity with the overall production term P_ω. The budget of the other two direction components is opposite and tends to cancel each other. This phenomenon can be also found in the stable laminar rotating thermal plumes, where the vortex transport equation is employed in the cylindrical coordinate system.[49] Moreover, the budgets of the tilting ($\omega_z \omega_r \frac{\partial V_z}{\partial r}$ and $\omega_z \omega_\theta \frac{\partial V_z}{r\partial \theta}$, i.e., $P_{\omega 3\_1}$ and $P_{\omega 3\_2}$) and stretching terms ($\omega_z \omega_z \frac{\partial V_z}{\partial z}$, i.e., $P_{\omega 3\_3}$) of $P_{\omega 3}$ are plotted in Fig. 10(b), revealing that the stretching term plays a dominant role in maintaining the high-intensity entrainment of the vortex. Although the other two terms (tilting terms) fluctuated during the transportation, they eventually converged to zero. These two terms are tilted by radial and tangential velocity gradients ($\frac{\partial V_z}{\partial r}$ and $\frac{\partial V_z}{r\partial \theta}$) during the transportation process and shifted from ω_r and ω_θ to ω_z.[20, 49]

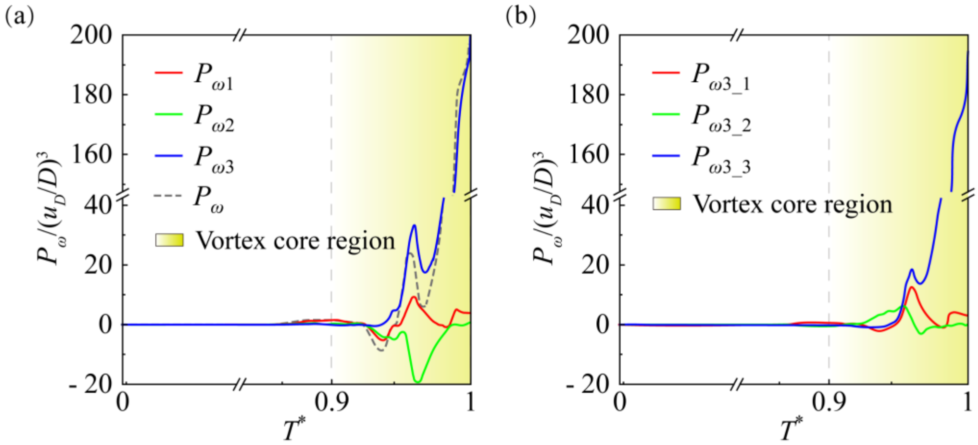

Fig. 9. Budgets of production term: (a) the radial, tangential, and axial direction components of P_ω and (b) the tilting and stretching components of $P_{\omega 3}$.

Removing the communal terms ω_z in $P_{\omega 3}$, the physical meaning of three items ($\omega_z \omega_r \frac{\partial V_z}{\partial r}$, $\omega_z \omega_\theta \frac{\partial V_z}{r\partial \theta}$ and $\omega_z \omega_z \frac{\partial V_z}{\partial z}$) can be clarified: $\omega_r \frac{\partial V_z}{\partial r}$ and $\omega_\theta \frac{\partial V_z}{r\partial \theta}$ represent the tilting effect of radial and tangential velocity gradients on radial vorticity and tangential vorticity respectively. $\omega_z \frac{\partial V_z}{\partial z}$ represents the stretching effect of the axial velocity gradient on the axial vorticity. Fig. 10(a) shows the process in which the radial and tangential vortices are distorted by the velocity gradients ($\frac{\partial V_z}{\partial r}$ and $\frac{\partial V_z}{r\partial \theta}$) and tilt toward the axial vortex. Red, green, and blue columns represent radial, tangential, and axial vortices, respectively. The dashed and solid columns represent the early and late stages of the vortices, respectively. The vortex evolution in Fig. 10(a) shows that, under the action of the velocity gradient, ω_r and ω_θ will eventually transform into ω_z. Fig. 10(b) shows vortex structures from the simulation results. The flow structure near the FSV is visualized by using the Q-criterion and dyed by ω^2, which demonstrates how radial and tangential vortices spiral and merge into the FSV center due to the influence of the velocity gradient tilting terms. These results do not only provide strong support for the previous discussion regarding the transformation of vortices with different directions but also exhibit a consistent evolution with the LCS observed in Fig. 7.

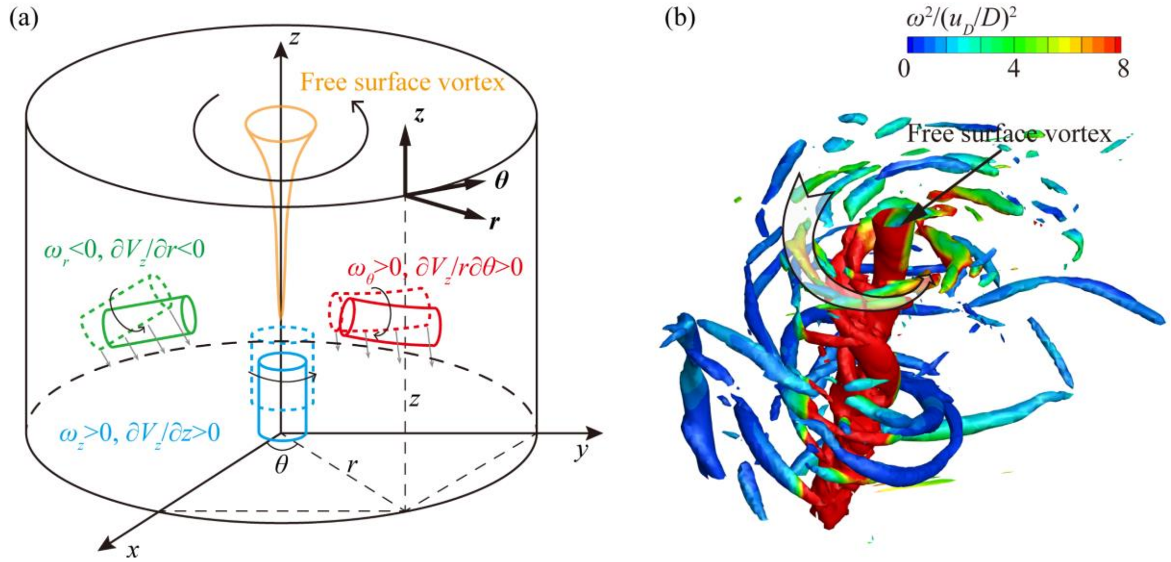

Fig. 10. (a) schematics of distortion effect from the velocity gradients and (b) vortex structures (iso-surface of $QD^2/u_D^2 = 5.5$).

5 Conclusions

The LES turbulence model with the CLSVOF method has been used to simulate the FSV phenomenon in the sewage pumping station. Based on these comprehensive flow fields, the transport and mixing characteristics of floating particles are studied when there is a FSV at the sump. The main results are the following:

(1) The spiral vortex band induced by FSV is studied for the first time and decomposed by the POD method. Two coherent structures have been identified: FSV represented by the first two high-energy orders, exceeding half of the total resolved turbulent energy, and the spiral vortex band represented by the low-energy higher orders, which consists of numerous small-scale vortices with different rotation directions.

(2) The LCS approach together with particle tracking is applied to reveal the evolution of the LCS and particle transport in the sump. LCS can be well captured by the FTLE method. As the LCS flows towards the FSV center,

it undergoes significant elongation by forming an elongated spiral shape before ultimately converging at the vortex center. Particles at different positions in the sump are first caught by the dividing line formed by FTLE ridges, mixed in the entrainment zone, then move along the FTLE ridge pathways and spiral into the vortex center of the sump. Eventually, they are drawn into the intake pipe and discharged in conjunction with the movement of the vortex.

(3) The dynamic spiral motion of particles is analyzed using the enstrophy transport equation in cylindrical coordinates to fully understand the entrainment mechanism of FSV on particles. It can be found that the dominant term responsible for the vortex entrainment of particles is the production term, which increases as a result of the stretching of the axially moving flow. The vorticity in the other two directions is converted into axial vorticity due to the inclination of the velocity gradient, further enhancing the entrainment effect of FSV on the particles in the vortex core region and accelerating the particle motion towards the pipe mouth.

The analytical methods used in this study have proven to be effective tools for predicting transport capacity and understanding the mechanisms of the FSV. The research results can provide a reference for the renovation design of existing sewage pumping stations and the operation of various urban drainage pumping stations. Furthermore, the design specifications for pumping stations can be supplemented and improved regarding the accumulation of floating debris in the sump. When utilizing FSV for FOG removal, the velocity gradients in the sump should be enhanced, for example by adjusting valves to lower the submergence or by activating additional units to increase the flow rate. The properties of FOG particles (e.g., composition and shape) influence their transport and mixing processes induced by FSV, a topic that warrants further exploration in future studies.

Acknowledgments

This work was supported by the National Natural Science Foundation of China (52379086; 52009033), the Jiangsu Innovation Support Programme for International Science and Technology Cooperation (BZ2023047), the Postdoctoral Research Foundation of China (2022T150185; 2022M711021). The computational work was supported by the High-Performance Computing Platform at Hohai University. The support of Hohai University is also gratefully acknowledged.

References

1. A. M. Moreno-Rodenas, A. Duinmeijer, andF. Clemens, "Deep-learning based monitoring of FOG layer dynamics in wastewater pumping stations," Water Res. **202**, 13 (2021).
2. A. Duinmeijer, andF. Clemens, "An experimental study on the motion of buoyant particles in the free-surface vortex flow," Journal of Hydraulic Research 1 (2021).
3. H. H. Yusuf, F. Roddick, V. Jegatheesan, L. Gao, andB. K. Pramanik, "Tackling fat, oil, and grease (FOG) build-up in sewers: Insights into deposit formation and sustainable in-sewer management techniques," Sci Total Environ **904**, 18 (2023).

4. S. P. A. Duinmeijer, "On the free-surface vortex driven motion of buoyant particles," PhD thesis, Delft University of Technology, Delft, The Netherlands, 2020.
5. G. E. Hecker, *Fundamentals of vortex intake flow* (Routledge, 2017).
6. W. J. M. Rankine, *A manual of applied mechanics* (Griffin, London, 1858).
7. J. M. Burgers, *A mathematical model illustrating the theory of turbulence* (1948).
8. A. Škerlavaj, L. Škerget, J. Ravnik, andA. Lipej, "Predicting free-surface vortices with single-phase simulations," Engineering Applications of Computational Fluid Mechanics **8**, 193 (2014).
9. V. Naderi, J. Yang, C. Lin, M. H. Kuo, andC. F. Hu, *There-dimensional velocity measurement on free surface of air-core intake vortex under critical submergence* (Egmond aan Zee, The Netherlands, 2016).
10. S. P. A. Duinmeijer, A. M. Moreno-Rodenas, M. Lepot, C. van Nieuwenhuizen, I. Meyer, andF. Clemens, "A simple measuring set-up for the experimental determination of the dynamics of a large particle in the 3D velocity field around a free surface vortex," Flow Measurement And Instrumentation **65**, 52 (2019).
11. H. Y. Cheng, X. R. Bai, X. P. Long, B. Ji, X. X. Peng, andM. Farhat, "Large eddy simulation of the tip-leakage cavitating flow with an insight on how cavitation influences vorticity and turbulence," Applied Mathematical Modelling **77**, 788 (2020).
12. X. L. Hou, J. P. Yuan, Y. X. Fu, R. Lu, J. L. Shi, andP. Y. Zhang, "A study on the dynamic characteristics of surface suction vortices in an open inlet pool," Physics of Fluids **35**, 16 (2023).
13. M. Hashid, andT. I. Eldho, "Numerical simulation of air-core surface vortex at critical submergence for dual horizontal intakes," Journal of Fluids Engineering **145**, 15 (2023).
14. G. Haller, "Lagrangian Coherent Structures," Annual Review of Fluid Mechanics **47**, 137 (2015).
15. A. Hadjighasem, M. Farazmand, D. Blazevski, G. Froyland, andG. Haller, "A critical comparison of Lagrangian methods for coherent structure detection," Chaos **27**, (2017).
16. A. Schneider, D. Conrad, andM. Böhle, "Lattice Boltzmann Simulation of the Flow Field in Pump Intakes—A New Approach," Journal of Fluids Engineering **137**, (2015).
17. S. B. Pope, *Turbulent Flows* (Cambridge University Press, Cambridge, 2000).
18. M. L. Shur, P. R. Spalart, M. K. Strelets, andA. K. Travin, "A hybrid RANS-LES approach with delayed-DES and wall-modelled LES capabilities," International Journal of Heat and Fluid Flow **29**, 1638 (2008).
19. X. Sun, W. X. Li, Q. Y. Huang, J. Zhang, andC. C. Sun, "Large eddy simulations of wind loads on an external floating-roof tank," Engineering Applications of Computational Fluid Mechanics **14**, 422 (2020).
20. Z. Li, H. Chen, H. Xu, J. Feng, K. Kan, T. Li, andL. Shen, "Effects of discharge-to-submergence ratio on evolution of air-core vortex," Ocean Engineering **281**, 114830 (2023).
21. X. Huang, Q. Guo, B. Qiu, andX. Feng, "Prediction of air-entrained vortex in pump sump: influence of turbulence models and interface-tracking methods," Journal of Hydraulic Engineering **146**, 04020010 (2020).
22. X. S. Wang, J. Zhang, Y. H. Chen, andZ. L. Kuai, "Numerical study of rising Taylor bubbles driven by buoyancy and additional pressure," International Journal of Multiphase Flow **159**, 12 (2023).
23. M. Sussman, P. Smereka, andS. Osher, "A level set approach for computing solutions to incompressible two-phase flow," Journal of Computational Physics **114**, 146 (1994).
24. K. Kan, Y. Xu, Z. Li, H. Xu, H. Chen, D. Zi, Q. Gao, andL. Shen, "Numerical study of instability mechanism in the air-core vortex formation process," Engineering Applications of Computational Fluid Mechanics **17**, 18 (2023).

25. M. Sussman, andE. G. Puckett, "A coupled level set and volume-of-fluid method for computing 3D and axisymmetric incompressible two-phase flows," Journal of Computational Physics **162**, 301 (2000).
26. H. Tse, "Challenges for pumping station design in water industries: An overview of impacts from climate change and energy crisis," Water Res. **253**, 21 (2024).
27. X. Song, Y. Luo, andZ. Wang, "Numerical prediction of the influence of free surface vortex air-entrainment on pump unit performance," Ocean Engineering **256**, (2022).
28. K. Kan, Y. Zheng, H. Chen, D. Zhou, J. Dai, M. Binama, andA. Yu, "Numerical simulation of transient flow in a shaft extension tubular pump unit during runaway process caused by power failure," Renewable Energy **154**, 1153 (2020).
29. H. Chen, D. Zhou, K. Kan, J. Guo, Y. Zheng, M. Binama, Z. Xu, andJ. Feng, "Transient characteristics during the co-closing guide vanes and runner blades of a bulb turbine in load rejection process," Renewable Energy **165**, 28 (2021).
30. K. Kan, Z. Yang, P. Lyu, Y. Zheng, andL. Shen, "Numerical study of turbulent flow past a rotating axial-flow pump based on a level-set immersed boundary method," Renewable Energy **168**, 960 (2021).
31. Z. Li, H. Xu, J. Feng, H. Chen, K. Kan, T. Li, andL. Shen, "Fluctuation characteristics induced by energetic coherent structures in air-core vortex: The most complex vortex in the tidal power station intake system," Energy **288**, 129778 (2024).
32. G. Xia, W. You, S. Manickam, J. Y. Yoon, X. Xuan, andX. Sun, "Numerical simulation of cavitation-vortex interaction mechanism in an advanced rotational hydrodynamic cavitation reactor," Ultrasonics Sonochemistry **105**, 106849 (2024).
33. I. B. Celik, U. Ghia, P. J. Roache, C. J. Freitas, H. Coleman, andP. E. Raad, "Procedure for estimation and reporting of uncertainty due to discretization in CFD applications," Journal of Fluids Engineering **130**, (2008).
34. H. Y. Zhang, J. L. Liu, J. X. Wu, W. X. Jiao, L. Cheng, andM. B. Yuan, "Research on optimization of the bulb form of the bulb tubular pump device for a low-head agricultural irrigation pumping station," Agriculture-Basel **13**, 18 (2023).
35. G. Möller, M. Detert, andR. M. Boes, "Vortex-induced air entrainment rates at intakes," Journal of Hydraulic Engineering **141**, (2015).
36. A. Duinmeijer, G. Oldenziel, andF. Clemens, "Experimental study on the 3D-flow field of a free-surface vortex using stereo PIV," Journal of Hydraulic Research **58**, 105 (2019).
37. L. Sirovich, "Turbulence and the dynamics of coherent structures. Parts I–III," Quarterly of Applied Mathematics **45**, 561 (1987).
38. D. Zi, L. Shen, F. Wang, B. Wang, andZ. Yao, "Characteristics and mechanisms of air-core vortex meandering in a free-surface intake flow," International Journal of Multiphase Flow **152**, 104070 (2022).
39. G. Haller, "Lagrangian coherent structures from approximate velocity data," Physics of Fluids **14**, 1851 (2002).
40. R. Sampath, M. Mathur, andS. R. Chakravarthy, "Lagrangian coherent structures during combustion instability in a premixed-flame backward-step combustor," Phys. Rev. E **94**, 062209 (2016).
41. J. D. Eldredge, andK. Chong, "Fluid transport and coherent structures of translating and flapping wings," Chaos **20**, (2010).
42. Z. Wang, andI. Gursul, "Unsteady characteristics of inlet vortices," Experiments in Fluids **53**, 1015 (2012).
43. C. Del Pino, J. M. Lopez-Alonso, L. Parras, andR. Fernandez-Feria, "Dynamics of the wing-tip vortex in the

near field of a NACA 0012 aerofoil," Aeronaut. J. **115**, 229 (2011).

44. S. C. Shadden, F. Lekien, andJ. E. Marsden, "Definition and properties of Lagrangian coherent structures from finite-time Lyapunov exponents in two-dimensional aperiodic flows," Physica D: Nonlinear Phenomena **212**, 271 (2005).
45. T. Watanabe, Y. Sakai, K. Nagata, Y. Ito, andT. Hayase, "Wavelet analysis of coherent vorticity near the turbulent/non-turbulent interface in a turbulent planar jet," Physics of Fluids **26**, (2014).
46. N. Sultana, F. Roddick, B. Jefferson, L. Gao, D. Bergmann, J. Papalois, M. Guo, K. Tzimourtas, andB. K. Pramanik, "Effectiveness of grease interceptors in food service establishments for controlling fat, oil and grease deposition in the sewer system," Sci Total Environ **912**, 12 (2024).
47. M. M. Neamtu-Halic, D. Krug, G. Haller, andM. Holzner, "Lagrangian coherent structures and entrainment near the turbulent/non-turbulent interface of a gravity current," Journal of Fluid Mechanics **877**, 824 (2019).
48. C. C. Tseng, andH. A. Hu, "Flow Dynamics of a Pitching Foil by Eulerian and Lagrangian Viewpoints," Aiaa J. **54**, 712 (2016).
49. F. C. Martins, J. M. C. Pereira, andJ. C. F. Pereira, "Vorticity transport in laminar steady rotating plumes," Physics of Fluids **32**, (2020).